Check for updates

*Advanced Materials*

ADVANCED MATERIALS
www.advmat.de

RESEARCH ARTICLE

# One-Step Direct Writing and In Situ Poling of Ultrathin Piezoelectric Microarchitectures for Organ-Conformal Stretchable Biointerfaces

Guo Tian[1,2] | Weili Deng[1] | Li'ang Zhou[1] | Tao Yang[1] | Boling Lan[1] | Shenglong Wang[1] | Yue Sun[1] | Yong Ao[1] | Tianpei Xu[1] | Longchao Huang[1] | Long Jin[1] | Weiqing Yang[1,3] | Ghim Wei Ho[2,4]

[1]Key Laboratory of Advanced Technologies of Materials (Ministry of Education), School of Materials Science and Engineering, Southwest Jiaotong University, Chengdu, P. R. China | [2]Department of Electrical and Computer Engineering, National University of Singapore, Singapore, Singapore | [3]Research Institute of Frontier Science, Southwest Jiaotong University, Chengdu, P. R. China | [4]Department of Materials Science and Engineering, National University of Singapore, Singapore, Singapore

**Correspondence:** Weili Deng (weili1812@swjtu.edu.cn) | Weiqing Yang (wqyang@swjtu.edu.cn) | Ghim Wei Ho (elehgw@nus.edu.sg)

**Received:** 10 February 2026 | **Revised:** 22 May 2026 | **Accepted:** 15 July 2026

**Keywords:** bioelectronics | electrohydrodynamic printing | gastrointestinal monitoring | personalized healthcare | piezoelectric materials | pressure sensor

## ABSTRACT

The development of ultrathin, stretchable piezoelectric biointerfaces is fundamentally constrained by the lack of manufacturing strategies capable of simultaneously delivering precise microarchitectural patterning and stable polarization in mechanically compliant formats. Here, we report a one-step electrohydrodynamic (EHD) direct-writing strategy with in situ poling, enabling the concurrent fabrication and polarization of free-standing, ultrathin piezoelectric microarchitectures without post-processing. By coupling this manufacturing approach with a mechanism-guided design based on thermoplastic polyurethane (TPU) and piezoelectric P(VDF-TrFE) through controlled modulation of EHD deposition and polymer crystallization, we manipulate grain size and flatten the polarization barrier by introducing structural heterogeneity to achieve a high and stable piezoelectric coefficient of 34.5 pm $V^{-1}$ in a highly stretchable architecture. The resulting sub-20 μm serpentine microarchitectures exhibit excellent mechanical compliance, long-term piezoelectric stability and deterministic architectural programmability. Integration with a breathable, controlled-adhesion elastomeric biointerface ensures robust conformal coupling to soft, wet tissue. Ex vivo demonstrations validate reliable detection and classification of gastric mechanical states, highlighting a manufacturing-enabled platform for organ-conformal piezoelectric biointerfaces. This work offers a generalizable strategy to overcome long-standing trade-offs between piezoelectric performance, stretchability, and ultrathin form factors, paving the way for diverse applications in biointegrated electronics and soft sensing, and healthcare systems.

## 1 | Introduction

Ultrathin, stretchable piezoelectric biointerfaces hold significant promise for seamless, conformal integration of electronics with soft, dynamic organs, enabling continuous monitoring of mechanical activity in physiological biological environments [1–6]. Such platforms are particularly attractive for biomedical applications, where mechanical signals encode rich information about organ function, motility, and health status [7–11]. Despite rapid progress in flexible and wearable electronics, the realization of truly organ-conformal piezoelectric systems remains fundamentally constrained by materials manufacturing challenges rather than device concepts alone, particularly the difficulty of simultaneously achieving precise microarchitectural

All rights reserved, including rights for text and data mining and training of artificial intelligence technologies or similar technologies.
© 2026 Wiley-VCH GmbH

patterning, stable piezoelectric polarization, and mechanical compliance in ultrathin formats [12–16]. Piezoelectric polymers, most notably poly(vinylidene fluoride)-based materials, are well suited for biointerfacing due to their intrinsic flexibility, biocompatibility, and ability to transduce mechanical deformation into electrical signals without external power sources [17–23]. Nevertheless, conventional fabrication routes, including blade coating, spin coating, hot pressing, and electrospinning, typically produce continuous films or fiber mats that lack architectural programmability. More critically, these approaches require separate, high-field electrical poling steps to induce piezoelectricity [24–27]. These post-processing steps are often incompatible with ultrathin, stretchable geometries and can lead to non-uniform polarization, mechanical damage, or long-term performance instability [28, 29]. As a result, scalable and reliable strategies for fabricating ultrathin, polarized piezoelectric microarchitectures remain limited.

Beyond fabrication limitations, intrinsic materials-level challenges further complicate the design of stretchable piezoelectric systems [30, 31]. Enhancing mechanical compliance often necessitates soft polymer incorporation, which tends to disrupt ferroelectric ordering and reduce remanent polarization. Consequently, improvements in stretchability frequently come at the expense of piezoelectric performance. Although this trade-off is well recognized, most existing strategies address it empirically rather than through a mechanism-guided design framework that explicitly considers the interplay between ferroelectric domain size, polarization magnitude, and polarization switching barrier to maximize effective piezoelectric response [32–34]. Overcoming this limitation requires an integrated approach that couples processing, materials chemistry, and domain structure design.

Here, we introduce a one-step electrohydrodynamic (EHD) direct-writing strategy with in situ poling that enables the simultaneous patterning and polarization of ultrathin piezoelectric microarchitectures without post-processing. The strong local electric field generated during EHD jetting aligns dipoles in real time during deposition, producing intrinsically polarized piezoelectric architectures directly in their final form. This material manufacturing approach allows deterministic writing of serpentine microarchitectures with sub-10-μm piezoelectric layers, combining architectural programmability, uniform polarization and mechanical compliance in ultrathin formats. To complement this fabrication strategy, we develop a mechanism-guided materials design based on TPU/P(VDF-TrFE) composites, in which the trade-off between domain size and polarization barrier is systematically tuned. By introducing soft thermoplastic polyurethane chains at controlled concentrations, the heterogeneous nucleation during printing leads to reduced grain size while preserving sufficient ferroelectric ordering, thereby maximizing the effective piezoelectric coefficient. This rational materials design yields a high and stable piezoelectric coefficient of 34.5 pm $V^{-1}$ in a highly stretchable composite, maintaining performance over 30 days. The resulting ultrathin piezoelectric microarchitectures are further integrated with a breathable, controllably adhesive elastomeric biointerface that enables robust, conformal coupling to soft, wet tissue. The combined architecture exhibits excellent mechanical compliance, stable electromechanical transduction, and reliable signal acquisition under large, reversible deformation. As a proof-of-concept demonstration of functional relevance, ex vivo studies validate the platform's ability to detect and classify gastric mechanical states when integrated with machine-learning. More broadly, this work establishes a manufacturing-enabled platform for organ-conformal piezoelectric biointerfaces, in which one-step direct writing with in situ poling, mechanism-guided ferroelectric polymer design, and microarchitectural design converge to overcome long-standing limitations in ultrathin, stretchable piezoelectric systems.

## 2 | Results and Discussion

### 2.1 | Structure Design and EHD Printing of the Ultrathin-Stretchable Piezoelectric Sensor

The serpentine TPU/P(VDF-TrFE) piezoelectric microarchitecture was fabricated by one-step EHD direct writing (Figure 1a). During jetting, the localized DC electric field established between the nozzle and the conductive substrate not only overcomes surface tension to form a stable Taylor cone, but also aligns dipoles of P(VDF-TrFE) chain, thereby enabling in situ poling [35, 36]. Simultaneously, electric field-induced stretching generates elongated fibers with enlarged specific surface area. Coupled with the fast evaporation of volatile mixed solvent (*N*,*N*-dimethylformamide and acetone), this promotes rapid solidification and confined crystallization of polymer within the printed fibers. Owing to the steric hindrance of the -TrFE group, the P(VDF-TrFE) preferentially crystallizes into the polar $\beta$ phase, forming intrinsically piezoelectric microstructures. To further verify the in situ poling during the EHD printing process, piezoelectric force microscopy (PFM) and quasi-static piezoelectric coefficient measurements were performed on both printing film and cast film (Figure S1). While both types of film showed homogeneous phase mapping images, local PFM spectroscopy revealed that only the EHD printed film exhibited hysteresis phase switching and a typical butterfly-shaped amplitude response. In contrast, the cast film showed nearly linear amplitude response, which may be attributed to electrostatic interaction between the tip and the sample surface rather than from piezoelectric response of P(VDF-TrFE). Consistently, the printed film showed a $d_{33}$ of about 36.3 pC $N^{-1}$, whereas the cast film did not display obvious piezoelectric response. These results provide direct evidence for effective in situ poling during the direct-writing process.

To understand and optimize the electromechanical response, we further elucidate the TPU-manipulated crystallization from a mechanism-guided perspective. According to classic nucleation theory, crystallization is governed by the competition between volume ($\Delta G_V$) and surface ($\Delta G_S$) free energies. Compared with the homogeneous P(VDF-TrFE) system, the incorporation of TPU creates heterogeneous interfaces that reduce the effective interfacial energy and decrease the critical nucleation radius ($r_c$), leading to higher nucleation density (Figure 1b). This microstructural regulation refines crystalline grains and ferroelectric domains, balancing the polarization and its switching barrier to regulate piezoelectricity (Figure 1c). It is noted that this benefit is non-monotonic; excessive interfacial disruption will suppress long-range ferroelectric ordering, driving a transition from ferroelectric to paraelectric behaviors and diminishing piezoelectricity. Therefore, optimizing the composite component



15214095, 2026, 53, Downloaded from https://advanced.onlinelibrary.wiley.com/doi/10.1002/adma.74367 by Jilin University, Wiley Online Library on [07/11/2026]. See the Terms and Conditions (https://onlinelibrary.wiley.com/terms-and-conditions) on Wiley Online Library for rules of use; OA articles are governed by the applicable Creative Commons License

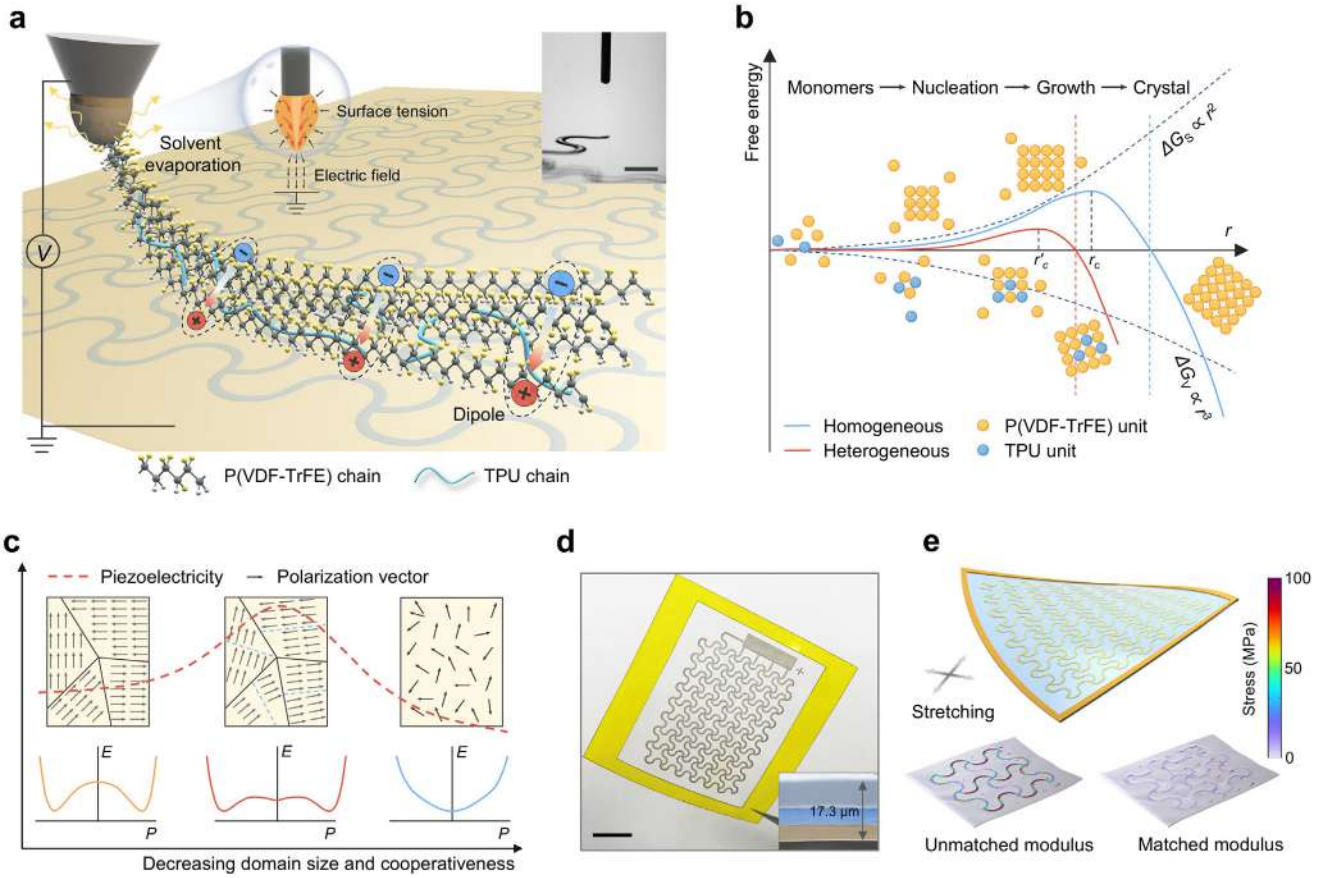



**FIGURE 1** | One-step fabrication and mechanical design of ultrathin piezoelectric microarchitectures. (a) Schematic illustration of the one-step EHD printing to fabricate intrinsically piezoelectric stretchable architectures; inset shows the optical microscope of needle and jet during printing (Scale bar is 2 mm). (b) Illustration of free energy profile as a function of crystal radius ($r$) in nucleation theory. $\Delta G_V$, $\Delta G_S$, and $r_c$ represent volume, surface free energies, and critical radius, respectively. (c) Phenomenological illustration of the piezoelectricity in different ferroelectric systems with structural heterogeneity. $P$ and $E$ represent polarization and free energy. (d) Photograph of the printed free-standing, ultrathin and stretchable piezoelectric device; inset shows cross-sectional morphology of the device (Scale bar is 1 cm). (e) Illustration of stretched device, and simulation results of stress distribution in the serpentine piezoelectric film-substrate composite system, with different modulus of the serpentine layer.

provides a rational route for maximizing piezoelectricity in the printed ultrathin, stretchable architectures.

Building upon the EHD-printed, intrinsically polarized serpentine architecture, a polydimethylsiloxane (PDMS) layer was subsequently spin-coated onto the polymer network to serve as a transfer substrate for delaminating the piezoelectric layer (Figure S2). In addition, an ethoxylated polyethyleneimine (PEIE)-modified PDMS layer was introduced as both the encapsulation and adhesion layer, enabling a robust and cohesive interface between the ultrathin-stretchable piezoelectric sensor and biotissue. An optical photograph of the printed device is shown in Figure 1d, where the synergistic integration of the serpentine geometry and elastic substrate endows the device with excellent flexibility and stretchability. A representative cross-sectional view of the device (Figure S3a–c and inset in Figure 1d) reveals an overall thickness of less than 20 μm, enabling intimate and conformal attachment to curved surfaces (Figure S3d). The incorporation of soft TPU chains also effectively reduces the elastic modulus of P(VDF-TrFE) [37], thereby alleviating the local stress concentration arising from the mechanical mismatch between the piezoelectric layer and elastic substrate during deformation, as confirmed by simulated stress distribution (Figure 1e). This combined structural and materials-level design enhances mechanical compliance and mitigates interfacial failure during prolonged operation.

## 2.2 | Piezoelectric Performance and Regulation Mechanism of the Printed Architecture

The incorporation of soft TPU chains leads to partial co-crystallization with P(VDF-TrFE), where the TPU segments are embedded within the polymer lamellar, acting as physical pinning sites that disrupt the formation of large crystalline domains (Figure 2a) [30]. This embedded structure effectively reduces the lamellar stiffness, thereby improving the flexibility and elasticity of the polymer composite. As a result, the tensile modulus decreases from 1.10 GPa for pristine P(VDF-TrFE) to 0.52 GPa at a TPU content of 25 wt%, while the elongation at break increases from 15.36% to 113.33% (Figure S4). More importantly, TPU chains also change the structure and continuity of the ferroelectric phase, which directly affects the effective electromechanical response of the composite. Since the piezoelectricity of P(VDF-TrFE) mainly originates from polarization of ferroelectric dipoles under mechanical stimulation rather than



15214095, 2026, 53, Downloaded from https://advanced.onlinelibrary.wiley.com/doi/10.1002/adma.74367 by Jilin University, Wiley Online Library on [07/11/2026]. See the Terms and Conditions (https://onlinelibrary.wiley.com/terms-and-conditions) on Wiley Online Library for rules of use; OA articles are governed by the applicable Creative Commons License

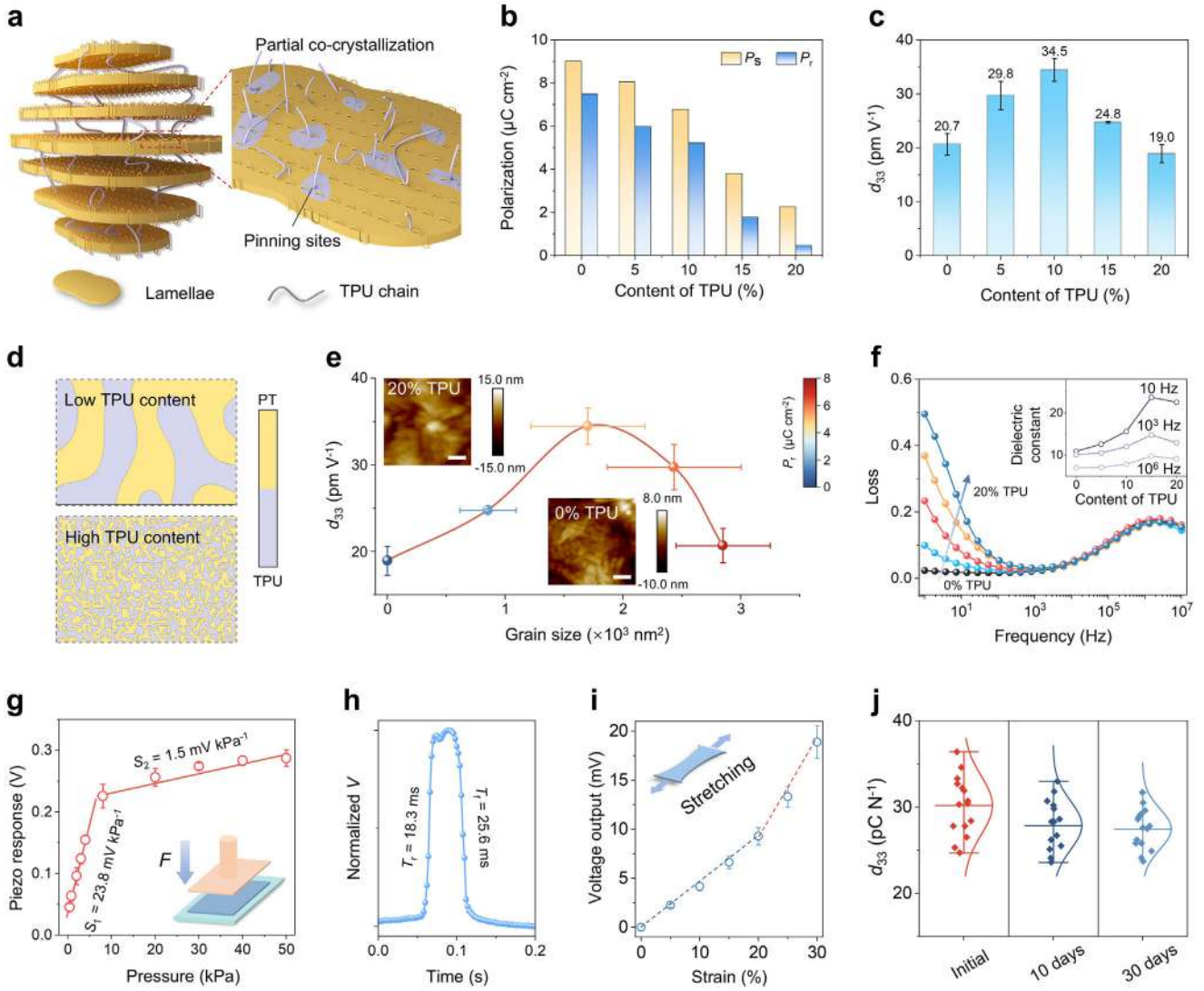



**FIGURE 2** | Mechanism-guided optimization of piezoelectric composites and electromechanical performance measurement. (a) Structural illustration of the polymer lamellar crystal comprising amorphous TPU chains (left part), enlarged schematic of partial co-crystallization shows disrupted ferroelectric ordering (upper right part). (b) Extracted saturated ($P_s$) and remanent ($P_r$) polarizations of composites with different TPU contents. (c) Piezoelectric coefficient ($d_{33}$) of the composites varying with TPU content. (d) Simulated distribution of polymer phases in the composite with different TPU contents. (e) Dependence between grain size, ferroelectric polarization, and piezoelectric coefficient in TPU/P(VDF-TrFE) composites. Insets present morphologies at different TPU contents (Scale bars are 100 nm). (f) Dielectric loss of samples versus frequency; the inset shows the extracted dielectric constant at selected frequencies. (g) Piezoelectric responses and calculated sensitivities at different pressure ranges. (h) Response time of the device under vertical loading, defined as the time of response signal from 10% to 90%. (i) Voltage responses of the device under various tensile strains. (j) $d_{33}$ of the piezoelectric composite before and after storage for 30 days (temperature = 25°C, relative humidity = 2%–3%).

carrier transport in composites, the key issue here is whether sufficient continuity of the ferroelectric phase can be maintained after TPU incorporation.

Furthermore, the effects of TPU incorporation on crystal structure and piezoelectricity were investigated (Figure 2b,c and Figures S5 and S6). FTIR results indicate that the incorporation of TPU does not alter the polar chain conformation of P(VDF-TrFE), whereas the XRD, DSC and morphological results reveal a pronounced effect on crystallization behavior (Figures S7 and S8). At low TPU content (<10 wt%), interfacial interactions and chain coupling promote heterogeneous nucleation, leading to refined grains and improved crystallinity. In this regime, P(VDF-TrFE) remains the dominant and continuous ferroelectric phase, so effective polarization can still be maintained. In addition, the reduction in grain size lowers the polarization switching barrier, which facilitates the piezoelectric response. At a TPU content of 10 wt%, the composite exhibits the highest piezoelectric coefficient (34.5 pm $V^{-1}$, Figure 2c). This performance remains competitive when considering its ultrathin form factor, stretchability, as well as the functionality (Table S1). Overall, the present system demonstrates a favorable balance between piezoelectric performance and device-level applicability.

With further increases in TPU content, the orderly packing of P(VDF-TrFE) chain is progressively hindered, thereby suppressing crystallization [38]. This evolution in crystallization behavior plays a key role in manipulating polarization and accompanying



15214095, 2026, 53, Downloaded from https://advanced.onlinelibrary.wiley.com/doi/10.1002/adma.74367 by Jilin University, Wiley Online Library on [07/11/2026]. See the Terms and Conditions (https://onlinelibrary.wiley.com/terms-and-conditions) on Wiley Online Library for rules of use; OA articles are governed by the applicable Creative Commons License

piezoelectricity. Phase-field simulations of the phase morphology indicate that the incorporation of high TPU content promotes heterogeneous nucleation and grain refinement (Figure 2d), thereby enabling effective modulation of the piezoelectricity. By correlating the piezoelectric performance with the grain size and polarization (Figure 2e), it is found that composites with relatively large grains exhibit limited piezoelectricity, which can be attributed to higher energy barrier of polarization switching. Upon reducing grain size through TPU incorporation (10 wt%), the polarization switching barrier decreases, facilitating domain activation and enhances the piezoelectricity (34.5 pm $V^{-1}$). With further increasing TPU content (20 wt%), the formation of discrete and finer grains is promoted. These fine grains cause a sharp decay in polarization, inducing a ferroelectric-to-paraelectric phase transition and ultimately reducing the piezoelectric response [32, 39, 40]. The dielectric results further support this interpretation (Figure 2f and Figure S9), where the increased dielectric loss and permittivity at low frequencies (< $10^3$ Hz) are indicative of increased interfacial regions arising from the finely divided crystalline domains [41, 42]. Therefore, the piezoelectricity of the TPU/P(VDF-TrFE) composite is determined not only by maximizing the intrinsic piezoelectric coefficient but also by balancing polarization capability with mechanical compliance. In this system, the incorporation of TPU modulates crystallization behavior, polarization switching barrier, and flexibility. Thus, TPU introduction is essential for achieving a mechanically compliant, stretchable, and tissue-conformal piezoelectric system while maintaining an appreciable electromechanical response.

To further evaluate piezoelectric performance of the designed TPU/P(VDF-TrFE) device, its electromechanical responses were investigated comprehensively. Pressure-voltage outputs of different composites with varying TPU contents were measured (Figure S10), showing strong agreement with the $d_{33}$ trends (Figure 2c). Notably, the 10 wt% TPU film yields a voltage response of 0.35 V under 50 kPa. The pressure sensitivity of the fabricated device was subsequently determined (Figure 2g and Figure S11), exhibiting an excellent value of 23.8 mV $kPa^{-1}$ in the low-pressure range of 1–10 kPa, which corresponds well to the typical physiological pressure range encountered in human or animal organs [43, 44]. Upon further increasing the applied pressure, the sensitivity decreases to 1.5 mV $kPa^{-1}$, which is attributed to strain saturation in the piezoelectric sensing layer. Meanwhile, the device exhibits a rapid dynamic response, with rise and fall times of 18.3 and 25.6 ms, respectively (Figure 2h). Considering that mechanical deformation in biological tissue typically involves a combination of stress and strain, the strain response of the device was further evaluated (Figure 2i and Figure S12). At small tensile strains, the device maintained a stable and nearly linear piezoelectric output, as the serpentine structure could release the strain through geometric unfolding. A stable voltage sensitivity of 0.47 mV/% was obtained within a strain range of 0%–20%. As the strain increases further, the piezoelectric response rises more markedly due to the larger overall deformation of the serpentine unit. The device also exhibited excellent cyclic tensile stability, with only a slight decrease in signal amplitude at the initial stage and nearly unchanged output during subsequent cycling (Figure S13a). Moreover, both the piezoelectric output and device morphology remained essentially stable after repeated loading cycles (Figures S13b,c), confirming its good mechanical durability and fatigue resistance. In addition, long-term stability tests confirm the robustness of the composite, as the piezoelectric coefficient remains unchanged after 30 days storage (Figure 2j). Overall, the printed architecture demonstrates strong and stable piezoelectric responses to both stress and strain, laying a solid foundation for reliable physiological mechanical activity monitoring.

## 2.3 | Wearable Performance and Biointerfacial Compatibility of the Device

To demonstrate the applicability of the printed ultrathin-stretchable piezoelectric sensor (UPS) on biological tissues, its wearability was systematically evaluated by analyzing adhesion, permeability and conformal deformation capabilities in biointerfaces. As illustrated in Figure 3a, the PDMS elastomer encapsulation was modified with PEIE to improve adhesion [45], leveraging hydrogen bonding between the abundant -OH groups of PEIE and biological tissue (Figure S14). Adhesion strengths of the pristine PDMS, PDMS/PEIE and commercial tape were compared to validate this design (Figure 3b, test method is shown in Figure S15). The modified PDMS/PEIE exhibits an adhesion strength of 10.5 kPa, representing a fivefold improvement over pristine PDMS (2.1 kPa) while remaining approximately half that of commercial tape (23.7 kPa). Moreover, repeated attachment-detachment tests show that the adhesion strength remains nearly unchanged over multiple cycles (Figure S16), confirming the stable interfacial adhesion of the device under sustained use. Such appropriately robust adhesion is crucial for wearable sensors to ensure conformal deformation and high-fidelity signal transduction, while avoiding excessive interfacial skin stress irritation. To assess the impact of adhesion on sensing performance, the piezoelectric responses of the UPS were investigated under different contact states (Figure 3c,d and Figure S17). By analyzing the potential, strain, and stress extracted from the marked traces, it was confirmed that conformal contact enables precise detection of substrate deformation. These results demonstrate that the PEIE-modified adhesion design significantly improves sensing fidelity of the UPS by ensuring stable mechanical coupling between the device and the underlying tissue.

Adhesion stability of the UPS was further validated under rigorous conditions. The UPS remained firmly attached to the skin during vigorous water rinsing, while an unmodified PDMS film detached easily (Figure 3e and Figure S18). To rigorously evaluate the device's stability in fluid environments, repeated washing tests were further performed. The piezoelectric voltage output before and after washing, as well as after multiple repeated washing cycles, showed negligible degradation in both response amplitude and signal profile (Figure 3f and Figure S19). This indicates that the device can maintain stable electromechanical performance under repeated aqueous exposure. Moreover, permeability of the UPS was evaluated (Figure S20), revealing a water vapor transmission rate (WVTR) of 1.32 kg $m^{-2}$ $d^{-1}$, significantly higher than that of a traditional P(VDF-TrFE) film (0.27 kg $m^{-2}$ $d^{-1}$) and exceeding the average permeability of human skin (~0.6 kg $m^{-2}$ $d^{-1}$). This enhanced breathability is expected to maintain skin comfort and minimize irritation during long-term monitoring [46, 47]. Mechanical stretchability was further evaluated using a balloon deformation test (Figure 3g), during which the UPS withstood strains of up to



15214095, 2026, 53, Downloaded from https://advanced.onlinelibrary.wiley.com/doi/10.1002/adma.74367 by Jilin University, Wiley Online Library on [07/11/2026]. See the Terms and Conditions (https://onlinelibrary.wiley.com/terms-and-conditions) on Wiley Online Library for rules of use; OA articles are governed by the applicable Creative Commons License

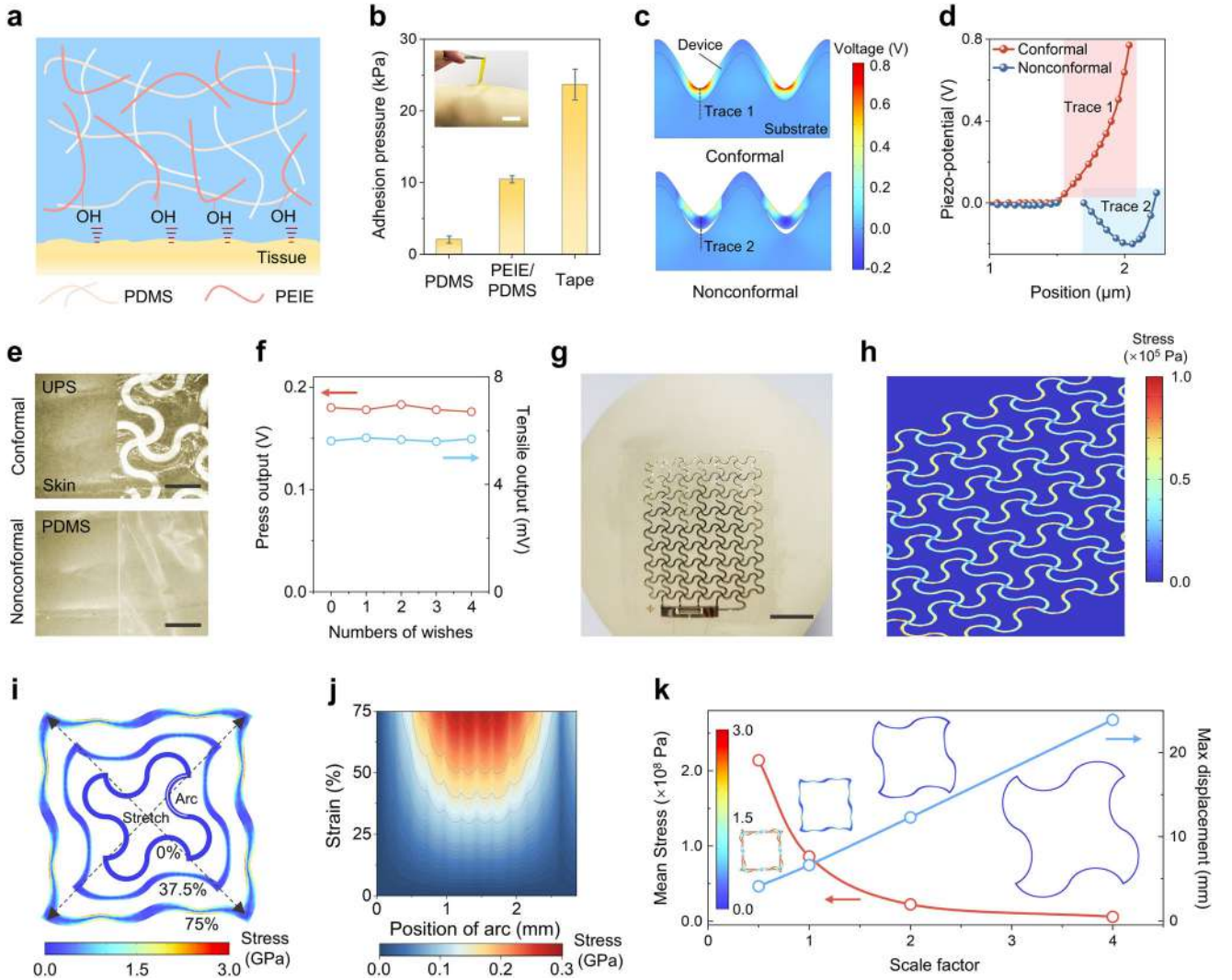



**FIGURE 3** | Characterizations of wearable performance and biointerfacial compatibility of the UPS. (a) Structural illustration of the PEIE-modified PDMS adhering to skin tissue through hydrogen bond interaction. (b) Adhesion strength of pristine PDMS, PEIE-modified PDMS, and commercial tape; the insert shows the peeling process of PEIE/PDMS from human skin (scale bar is 10 mm). (c) Simulation results of voltage responses during device stretching with different contact states. (d) Extracted voltage signal from figure (c) along the traces. (e) Optical images of the UPS and PDMS film attached to artificial skin after washing (scale bars are 500 μm). (f) Voltage responses of the device under pressure and tensile stimulus before and after repeated washing cycles. (g) Optical image of the UPS on an inflated balloon (Scale bar is 2 cm). (h) Simulated stress distribution in the device during inflating. (i) Simulated stress distribution of a single piezoelectric serpentine structure unit under different strains. (j) Calculated stress of the selected arc as marked in figure (i) with different strains. (k) Stress distribution, mean stress, and max displacement in a serpentine piezoelectric unit within different structural factors.

200% without structural failure. Finite element analysis (FEA) showed a uniform stress distribution under substrate stretching (Figure 3h), indicating that the serpentine network effectively dissipates energy and mitigates structural damage caused by local stress concentration [48]. In addition, FEA was performed to analyze the evolution of stress in the serpentine structure as a function of applied deformation (Figure 3i,j). For applied strain below 50%, deformation of the serpentine network is primarily accommodated by geometric unfolding, which enables the device to tolerate large overall deformation. The geometrical scale of the serpentine network plays a critical role in modulating both its deformability and piezoelectric response. Compared with the selected structural scale (scale factor = 1), larger unit sizes accommodate greater deformation but induce lower strain in the piezoelectric layer, resulting in a weaker electrical output, and vice versa (Figure 3k). Collectively, the combination of strong yet skin-friendly adhesion, high permeability, and excellent mechanical compliance of the UPS establishes a robust platform for stable and accurate monitoring of physiological mechanical information.

## 2.4 | Ex Vivo Assessment of Gastric Status Monitoring Using the UPS

Gastric mechanical activity provides direct insight into digestive dynamics and functional states of the stomach, making it an important physiological indicator for assessing gastrointestinal



15214095, 2026, 53, Downloaded from https://advanced.onlinelibrary.wiley.com/doi/10.1002/adma.74367 by Jilin University, Wiley Online Library on [07/11/2026]. See the Terms and Conditions (https://onlinelibrary.wiley.com/terms-and-conditions) on Wiley Online Library for rules of use; OA articles are governed by the applicable Creative Commons License

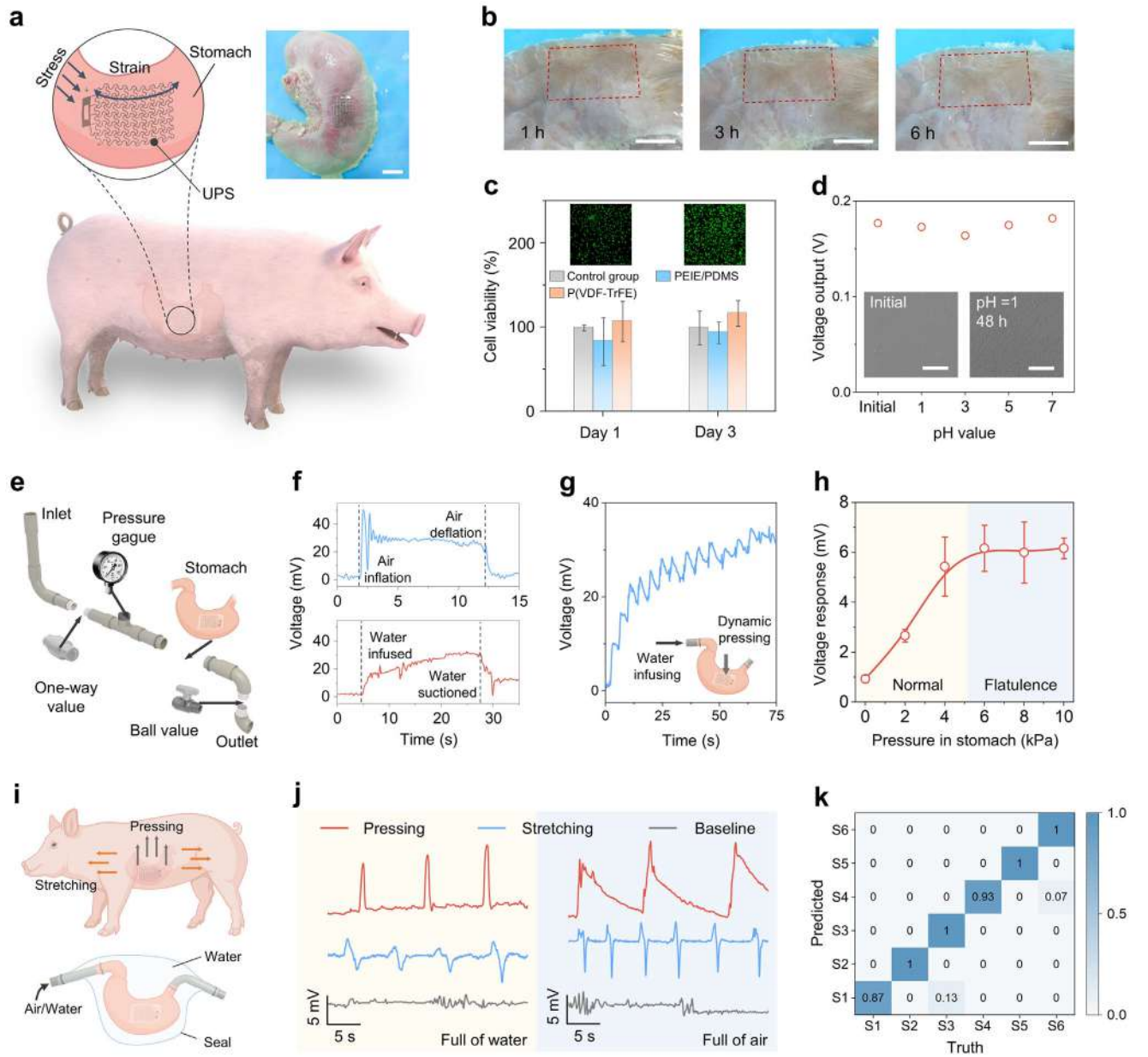



**FIGURE 4** | Ex vivo assessment of stomach physiological activity monitoring using the UPS. (a) Schematic illustration of gastric motility monitoring based on UPS and optical image of the UPS conformally attached to an ex vivo porcine stomach (scale bar is 3 cm). (b) Photography of the stomach after different attachment durations of the UPS (scale bars are 3 cm). (c) Live/dead fluorescence assay of cell cultured on the piezoelectric and the encapsulation layers for 72 h. (d) Voltage output of the UPS immersed in simulated gastric fluid with different pH values; inserts show the device morphology before and after exposure (scale bars are 4 μm). (e) Schematic illustration of the in vitro setup to simulate stomach activity under different physiological states. (f) Continuous voltage signals recorded by the UPS during the stomach infused with air or water. (g) Voltage response under dynamic pressure conditions, where fluctuating peaks correspond to continuous water infusion into the stomach. (h) Voltage response of the UPS under external pressing at various internal pressures, showing gradual signal saturation as the stomach bulges. (i) Schematic of the in vitro setup to stimulate gastric stress and strain. (j) Representative voltage responses under different stimuli applied to the stomach. (k) Identification of gastric physiological states based on collected signals; the labels S1–S6 correspond to combinations of two stimulations (pressing and stretching) under three stomach conditions: empty, water-filled, and air-filled, respectively.

function [49–51]. Accurate monitoring of gastric deformation and pressure variations requires soft and conformal bioelectronics capable of capturing subtle mechanical signals on compliant tissues [52, 53]. In this context, the UPS was applied as a proof-of-concept for gastric monitoring using an ex vivo model to distinguish different states of the stomach (Figure 4a). To evaluate the interfacial contact between the device and stomach tissue, adhesion tests were performed under simulated physiological wet conditions (Figure 4b and Figure S21). The device maintained long-term stable and reversible adhesion to the tissue surface without causing noticeable damage. In addition, the device remained stably attached to the tissue surface after immersion in simulated body fluid, and the measured adhesion strength (10.89 kPa) was comparable to that obtained under dry conditions



15214095, 2026, 53, Downloaded from https://advanced.onlinelibrary.wiley.com/doi/10.1002/adma.74367 by Jilin University, Wiley Online Library on [07/11/2026]. See the Terms and Conditions (https://onlinelibrary.wiley.com/terms-and-conditions) on Wiley Online Library for rules of use; OA articles are governed by the applicable Creative Commons License

(10.68 kPa), confirming its reliable adhesion in wet conditions (Figure S22). Cell viability and cytotoxicity tests of the UPS were further assessed (Figure 4c and Figure S23), and fluorescence images and quantitative cell viability analysis demonstrated that cells adhered and proliferated well on both the piezoelectric sensing layer and the encapsulation layer, supporting the good biocompatibility of the device. Chemical stability of the device was evaluated by immersing it in artificial tissue fluid of varying pH values for 48 h (Figure 4d). The device maintained stable piezoelectric voltage outputs without structural or functional degradation, confirming its operational robustness in a gastric fluid environment.

Furthermore, the sensing functionality of the UPS was evaluated using a balloon-based model to simulate gastric expansion (Figure S24). The device exhibits progressively enhanced piezoelectric signals with increasing pressure, enabling effective discrimination between normal and overexpanded states. To better emulate the physiological conditions, a dual-balloon configuration was employed to test external compression and different internal filling media (Figure S25). Distinctive signal responses of the UPS were obtained under different pressure levels and internal contents, demonstrating its potential for detecting gastric pressure states and internal conditions. Building on the balloon-based validation, an ex vivo porcine stomach system was constructed to assess device performance under more realistic conditions (Figure 4e and Figure S26). When the stomach was infused with air or water, characteristic signal responses demonstrate reliable discrimination of different internal contents (Figure 4f). Water infusion produced a gradually increasing voltage output associated with rising internal pressure, whereas air infusion resulted in an immediate voltage response followed by a stable signal, reflecting the distinct compressibility and pressure transmission behaviors of water and air. During water infusion, the piezoelectric signals exhibited a rising baseline corresponding to gastric swelling, superimposed with periodic voltage peaks arising from dynamic pressure fluctuations (Figure 4g). The gradual baseline shift further indicates the transition from an expanding state to a saturated gastric state (Figure 4h), confirming the capability of the UPS to simultaneously monitor both stress and strain signals during gastric activities.

Based on these results, an ex vivo stomach model was constructed by encapsulating a fresh porcine stomach with an elastic water-filled film to mimic physiological conditions (Figure 4i and Figure S27). This model allowed controlled mechanical stimulation through pressing and stretching, while the UPS recorded real-time electrical responses associated with gastric motility. Different signal patterns were observed for air-filled versus water-filled conditions, as well as under pressing or stretching stimuli (Figure 4j). In contrast, the empty stomach presented markedly lower signal amplitudes (Figure S28), as external stimuli were absorbed by the compliant device architecture. These characteristic response patterns enabled reliable identification of different gastric states. Moreover, the integration of the collected sensing signals with machine learning algorithms allowed classification of stomach conditions (empty, water-filled, and air-filled) with an accuracy of 96.7% (Figure 4k). The corresponding accuracy and loss curves converged rapidly within a few training epochs (Figure S29), indicating robust signal separability and efficient feature learning. Collectively, these ex vivo studies demonstrate that the UPS enables effective monitoring of gastric activities and states, offering a promising approach for real-time evaluation of stomach activity and potential diagnosis of feeding-related disorders.

## 3 | Conclusions

This work introduces a manufacturing-enabled paradigm and materials-driven design strategy for conformal piezoelectric biointerfaces by integrating EHD direct writing, in situ poling, and mechanism-guided ferroelectric polymer design. By coupling architectural patterning and real-time dipole alignment, this approach overcomes long-standing incompatibilities between mechanically compliant and ultrathin formats, thereby eliminating the need for post-poling steps. Beyond manufacturing processing, a rational materials strategy based on controlled incorporation of soft TPU chains into P(VDF-TrFE) regulates heterogeneous nucleation and grain size, balancing polarization and switching barrier of the ferroelectric domain, achieving a high, stable piezoelectric coefficient of 34.5 pm $V^{-1}$ over 30 days. After integrating with a breathable and controlled-adhesion elastomeric substrate, the resulting architecture exhibits excellent organ conformation and stable electromechanical transduction at soft, wet biointerfaces. The demonstrated gastric state monitoring serves as a proof-of-concept, highlighting the broader applicability of this approach for biointegrated sensing and diagnostic technologies.

The present study demonstrates promising performance in ultrathin, stretchable, and conformal piezoelectric biointerfaces, while highlighting its potential for future in vivo translation owing to its ultrathin format, mechanical compliance, conformability, and self-powered sensing capability. However, the current work remains primarily focused on materials design, manufacturing strategy, and proof-of-concept application demonstration. Further studies are needed to evaluate long-term performance and signal reliability in more complex physiological environments and to extend this work toward more realistic in vivo scenarios. In addition, the material system and device geometry could be further optimized for broader biomedical applications. Issues such as long-term biocompatibility and stable interfacing with more complex organ surfaces remain important directions for future research. Overall, this work provides a generalizable manufacturing strategy for ultrathin piezoelectric biointerfaces, opening new opportunities for piezoelectric polymers in bioelectronics, soft sensing, and personalized healthcare.

## 4 | Experimental Section

### 4.1 | Device Fabrication of the UPS

P(VDF-TrFE) and TPU were purchased from Arkema (Piezotech, 70/30) and BASF (1170A), respectively. The P(VDF-TrFE) was dissolved in a mixture *N*,*N*-dimethylformamide/acetone (50/50 wt%) at a concentration of 15 wt% and stirred for 6 h at room temperature. The TPU was added with selected concentration and stirred for 6 h to obtain a homogeneous solution for printing. An EHD printer was utilized to fabricate the polymer serpentine



15214095, 2026, 53, Downloaded from https://advanced.onlinelibrary.wiley.com/doi/10.1002/adma.74367 by Jilin University, Wiley Online Library on [07/11/2026]. See the Terms and Conditions (https://onlinelibrary.wiley.com/terms-and-conditions) on Wiley Online Library for rules of use; OA articles are governed by the applicable Creative Commons License

network. The solution was delivered using a syringe pump (10 μL $min^{-1}$) with a metal needle (25G), while a DC high voltage (~3 kV) was applied between the nozzle and the substrate to induce jetting fiber. The distance between the nozzle and the substrate was about 0.5–1 mm. These printing parameters were carefully optimized, as the applied voltage determines the formation and stability of the electrified jet and also contributes to dipole alignment during printing. The printed samples were then dried on a hotplate at 60°C for 3 h. Then, the magnetron sputtering was applied to deposit the Ag electrode with a patterned mask, where the electrode linewidth was smaller than that of the polymer trace to prevent short circuit.

To transfer the fabricated device, the PDMS (Dow Corning, Sylgard184) solution was prepared by mixing the base and curing (A:B = 10:1 in wt) in hexane (1:1 in wt). The mixture was ultrasonicated for 3 min to remove air bubbles, then it was spin-coated onto the printed serpentine structure at 500 rpm for 10 s and dried on a hotplate at 110°C for 10 min to form a solid PDMS film. A supporting frame (double-sided tape with a cover) was prepared by laser cutting and attached to the PDMS surface. The film was then gently peeled off from the substrate with the support frame, and a back electrode was deposited on the opposite side by sputtering. Next, a PDMS/hexane solution containing PEIE (0.4 wt% to PDMS) was prepared and spin-coated onto a Teflon substrate, followed by baking at 110°C for 30 s. Then, the fabricated film was uniformly spread onto this PEIE-modified layer and further baked at 110°C for 10 min to achieve solidification and encapsulation; then the entire device was detached from the Teflon substrate. For electrical measurement, silver wires were used to lead out the electrode and establish an electrical connection to the external circuit.

### 4.2 | Characterizations of the materials and devices

The morphologies and EDS distribution of elements were characterized by a scanning electron microscope (JSM 7800F), and the topographies of film with different TPU content were characterized by an AFM (Multimode 8, Bruker). For the grain size analysis shown in Figure 2e, the statistics were obtained based on AFM topographic images, and the sizes were analyzed using ImageJ software. Specifically, the AFM images were first processed to improve the visibility of grain boundaries, followed by grain identification and statistical analysis. For each AFM image, several tens of grains were typically counted, and the resulting grain-area distributions were presented in the form of histograms with fitted curves. The mechanical performance of the ultrathin film was tested by a universal tensile testing machine (LDW-1, Songdun Instrument). The chemical composite, crystal structure and degree of crystallinity were characterized by FTIR (scan resolution: 1 $cm^{-1}$, INVENIO, Bruker), XRD (Empyrean, PANalytical) and DSC (heating and cooling rate 10°C $min^{-1}$, Mettler Toledo). The ferroelectric and piezoelectric properties were measured through the TF Analyzer (2000E, aixACCT) equipped with an amplifier (Trek 610E) and a laser interferometer, in which the frequency of the electric field is 1 Hz. The dielectric constant and loss spectrum were tested by a broad dielectric spectrometer (Concept 80, Novocontrol) at room temperature. The polymer composite was printed into square sample (10 mm × 10 mm) for the ferroelectric and dielectric measurements. The electromechanical responses were tested using a low-noise voltage preamplifier (SR 560, Stanford Research System), a linear motor equipped with force probe (M7-50, Mark-10) was applied to load pressure; the sampling rate was fixed at 10000 Hz to measure response time.

### 4.3 | Biocompatibility Evaluation of the UPS

Fresh porcine stomach tissues were directly purchased from a slaughterhouse. After collection, the tissue was only gently rinsed with deionized water to remove residual gastric contents, without any additional treatment. The subsequent adhesion and sensing tests were then carried out directly on the stomach tissue surface. For the underwater adhesion test, the porcine stomach tissue was immersed in phosphate buffered saline (PBS) solution to alleviate tissue changes caused by osmotic imbalance. For the sensing tests, the tubes were directly connected to the stomach tissue and fixed with waterproof sealing tape. All experiments were conducted under indoor conditions (~25°C). Because the entire sensing test lasted for several days, the stomach tissue was stored at -20°C after use. Before reuse, the tissue was thawed in PBS solution prior to subsequent tests. The water vapor transmission rate (WVTR) of the device was measured using a home-made setup (Figure S20). The deionized water was placed into the container, and the sample was sealed over the opening. Then, the total weight of the setup was recorded at different times respectively over a period of 5 days. The WVTR was then calculated based on the weight loss of water over time. Cytotoxicity was assessed using a fibroblast cell line, the device was attached onto a glass substrate, which is used for cell adhesion and culture. The extract solution was collected and added to cell culture wells to incubate for a defined period. Then, live/dead fluorescence staining was performed to assess cell viability using a CCK-8 assay. To evaluate the stability of the device under gastric-like conditions, 200 mL of phosphate-buffered saline (PBS, pH ≈ 7.4) was adjusted to pH values of 1, 3, 5, and 7 using hydrochloric acid. The devices were immersed in these solutions for assessing durations, then rinsed with deionized water and used for piezoelectric performance testing to evaluate robustness after exposure.

#### Acknowledgements

This study was supported by the Natural Science Foundation of China (No. U2330120) and the Basic Research Cultivation Project of Southwest Jiaotong University (No. 2682023KJ024). Guo Tian gratefully acknowledges financial support from the China Scholarship Council. The authors also thank the help from the Analysis and Testing Center of Southwest Jiaotong University for characterization assistance.

#### Conflicts of Interest

The authors declare no conflicts of interest.

#### Data Availability Statement

The data that support the findings of this study are available from the corresponding author upon reasonable request.



15214095, 2026, 53, Downloaded from https://advanced.onlinelibrary.wiley.com/doi/10.1002/adma.74367 by Jilin University, Wiley Online Library on [07/11/2026]. See the Terms and Conditions (https://onlinelibrary.wiley.com/terms-and-conditions) on Wiley Online Library for rules of use; OA articles are governed by the applicable Creative Commons License

## References


1. J. Liu, N. Liu, Y. Xu, et al., "Bioresorbable Shape-Adaptive Structures for Ultrasonic Monitoring of Deep-Tissue Homeostasis," *Science* 383 (2024): 1096–1103, https://doi.org/10.1126/science.adk9880.

2. W. Deng, Y. Zhou, A. Libanori, G. Chen, W. Yang, and J. Chen, "Piezoelectric Nanogenerators for Personalized Healthcare," *Chemical Society Reviews* 51 (2022): 3380–3435, https://doi.org/10.1039/D1CS00858G.

3. Z. Zhang, J. Yang, H. Wang, et al., "A 10-Micrometer-Thick Nanomesh-Reinforced Gas-Permeable Hydrogel Skin Sensor for Long-Term Electrophysiological Monitoring," *Science Advances* 10 (2024): adj5389, https://doi.org/10.1126/sciadv.adj5389.

4. Z. Jiang, N. Chen, Z. Yi, et al., "A 1.3-Micrometre-Thick Elastic Conductor for Seamless on-Skin and Implantable Sensors," *Nature Electronics* 5 (2022): 784–793, https://doi.org/10.1038/s41928-022-00868-x.

5. M. Kaltenbrunner, T. Sekitani, J. Reeder, et al., "An Ultra-Lightweight Design for Imperceptible Plastic Electronics," *Nature* 499 (2013): 458–463, https://doi.org/10.1038/nature12314.

6. T. Ha, J. Tran, S. Liu, et al., "A Chest-Laminated Ultrathin and Stretchable E-Tattoo for the Measurement of Electrocardiogram, Seismocardiogram, and Cardiac Time Intervals," *Advanced Science* 6 (2019): 1900290, https://doi.org/10.1002/advs.201900290.

7. Y. Sun, G. Tian, W. Deng, and W. Yang, "Ionic Hydrogel Sensors Toward Next-Gen Personalized Healthcare," *Advanced Materials* 38 (2026): 09122.

8. W. Lu, W. L. Ong, X. Pan, Z. Li, G. Tian, and G. W. Ho, "Design Strategies and Roles of Hydrogels for Sustainable Energy Conversion and Harvesting From Natural and Biological Environments," *Advanced Materials* 37 (2025): 10270.

9. Z. Liu, G. Chen, M. S. Jo, et al., "Mechanomedicine," *Nature Reviews Bioengineering* 4 (2026): 216–235, https://doi.org/10.1038/s44222-025-00391-6.

10. M. Wang, K. Wei, Y. Shi, et al., "Frontiers of Advanced Multifunctional Liquid Metal – Wood Composite Materials," *Progress in Materials Science* 160 (2026): 101687, https://doi.org/10.1016/j.pmatsci.2026.101687.

11. G. Tian, L. Huang, X. Pan, et al., "Meta-Topological Hydrogel Enables Multisource and Frequency-Tailored Artefact Mitigation for Bioelectronics," *Nature Sensors* 1 (2026): 413–424, https://doi.org/10.1038/s44460-026-00055-x.

12. Z. Wang, S. Wang, B. Lan, et al., "Piezotronic Sensor for Bimodal Monitoring of Achilles Tendon Behavior," *Nano-Micro Letters* 17 (2025): 241, https://doi.org/10.1007/s40820-025-01757-6.

13. J. Liu, G. Tian, W. Yang, and W. Deng, "Recent Progress in Flexible Piezoelectric Devices Toward Human-Machine Interactions," *Soft Science* 2 (2022): 22.

14. Y. Yoon, P. L. Truong, D. Lee, and S. H. Ko, "Metal-Oxide Nanomaterials Synthesis and Applications in Flexible and Wearable Sensors," *ACS Nanoscience Au* 2 (2022): 64.

15. H. Kong, W. Li, Z. Song, and L. Niu, "Recent Advances in Multimodal Sensing Integration and Decoupling Strategies for Tactile Perception," *Materials Futures* 3 (2024): 022501, https://doi.org/10.1088/2752-5724/ad305e.

16. Z. Wang, J. Jiang, K. Wei, et al., "Advanced Cellulose-Based Gels for Wearable Physiological Monitoring: From Fiber Modification to Application Optimization," *Advanced Functional Materials* 36 (2026): 15132, https://doi.org/10.1002/adfm.202515132.

17. X. Qian, X. Chen, L. Zhu, and Q. M. Zhang, "Fluoropolymer Ferroelectrics: Multifunctional Platform for Polar-Structured Energy Conversion," *Science* 380 (2023): adg0902, https://doi.org/10.1126/science.adg0902.

18. H. Zhang, Y. Tang, Z. Gu, et al., "Biodegradable Ferroelectric Molecular Crystal With Large Piezoelectric Response," *Science* 383 (2024): 1492–1498, https://doi.org/10.1126/science.adj1946.

19. F. Yang, J. Li, Y. Long, et al., "Wafer-Scale Heterostructured Piezoelectric Bio-Organic Thin Films," *Science* 373 (2021): 337–342, https://doi.org/10.1126/science.abf2155.

20. G. Tian, W. Deng, T. Yang, et al., "Hierarchical Piezoelectric Composites for Noninvasive Continuous Cardiovascular Monitoring," *Advanced Materials* 36 (2024): 2313612.

21. G. Tian, L. Guo, Y. Gao, et al., "A Wearable All-In-One Obstructive Sleep Apnea Management System with Flexible Piezoelectric Monitoring and Soft Magnetoelastic Stimulating," *Matter* 8 (2025): 102323.

22. Y. Zhang, X. Hu, Z. Yan, et al., "Ultra-Soft Organic Combined Film With Piezoelectricity Induced by Liquid-Liquid Interface Polar Engineering," *Nature Communications* 16 (2025): 6410.

23. X. Kang, K. Jiang, S. Ge, et al., "Frontier in Advanced Luminescent Biomass Nanocomposites for Surface Anticounterfeiting," *ACS Nano* 19 (2025): 11547–11575, https://doi.org/10.1021/acsnano.4c17883.

24. C. Ribeiro, C. M. Costa, D. M. Correia, et al., "Electroactive Poly(vinylidene fluoride)-Based Structures for Advanced Applications," *Nature Protocols* 13 (2018): 681–704, https://doi.org/10.1038/nprot.2017.157.

25. P. Martins, A. C. Lopes, and S. Lanceros-Mendez, "Electroactive Phases of Poly(vinylidene fluoride): Determination, Processing and Applications," *Progress in Polymer Science* 39 (2014): 683–706, https://doi.org/10.1016/j.progpolymsci.2013.07.006.

26. W. Zhang, Y. Zhang, X. Yan, Y. Hong, and Z. Yang, "Challenges and Progress of Chemical Modification in Piezoelectric Composites and Their Applications," *Soft Science* 3 (2023): 19, https://doi.org/10.20517/ss.2022.33.

27. Y. Ao, L. Jin, S. Wang, et al., "Dual Structure Reinforces Interfacial Polarized MXene/PVDF-TrFE Piezoelectric Nanocomposite for Pressure Monitoring," *Nano-Micro Letters* 17 (2025): 320, https://doi.org/10.1007/s40820-025-01839-5.

28. Y. Wang, C. Huang, Z. Cheng, et al., "Halide Perovskite Inducing Anomalous Nonvolatile Polarization in Poly (vinylidene fluoride)-Based Flexible Nanocomposites," *Nature Communications* 15 (2024): 3943.

29. M. T. Chorsi, T. T. Le, F. Lin, et al., "Highly Piezoelectric, Biodegradable, and Flexible Amino Acid Nanofibers for Medical Applications," *Science Advances* 9 (2023): adg6075, https://doi.org/10.1126/sciadv.adg6075.

30. L. Gao, B. L. Hu, L. Wang, et al., "Intrinsically Elastic Polymer Ferroelectric by Precise Slight Cross-Linking," *Science* 381 (2023): 540–544, https://doi.org/10.1126/science.adh2509.

31. T. Tang, Z. Shen, J. Wang, et al., "Stretchable Polymer Composites With Ultrahigh Piezoelectric Performance," *National Science Review* 10 (2023): nwad177, https://doi.org/10.1093/nsr/nwad177.

32. F. Li, D. Lin, Z. Chen, et al., "Ultrahigh Piezoelectricity in Ferroelectric Ceramics by Design," *Nature Materials* 17 (2018): 349–354, https://doi.org/10.1038/s41563-018-0034-4.

33. X. Chen, H. Qin, X. Qian, et al., "Relaxor Ferroelectric Polymer Exhibits Ultrahigh Electromechanical Coupling at Low Electric Field," *Science* 375 (2022): 1418–1422, https://doi.org/10.1126/science.abn0936.

34. Y. Liu, H. Aziguli, B. Zhang, et al., "Ferroelectric Polymers Exhibiting Behaviour Reminiscent of a Morphotropic Phase Boundary," *Nature* 562 (2018): 96–100, https://doi.org/10.1038/s41586-018-0550-z.

35. Z. Zhang, X. Li, Z. Peng, et al., "Active Self-Assembly of Piezoelectric Biomolecular Films via Synergistic Nanoconfinement and In-Situ Poling," *Nature Communications* 14 (2023): 4094.

36. X. Li, Z. Zhang, Y. Zheng, et al., "One-Step High-Speed Thermal-Electric Aerosol Printing of Piezoelectric Bio-Organic Films for Wirelessly Powering Bioelectronics," *Science Advances* 10 (2024): adq3195.

37. N. Shehata, R. Nair, R. Boualayan, et al., "Stretchable Nanofibers of Polyvinylidenefluoride (PVDF)/Thermoplastic Polyurethane (TPU) Nanocomposite to Support Piezoelectric Response via Mechanical Elasticity," *Scientific Reports* 12 (2022): 8335, https://doi.org/10.1038/s41598-022-11465-5.




15214095, 2026, 53, Downloaded from https://advanced.onlinelibrary.wiley.com/doi/10.1002/adma.74367 by Jilin University, Wiley Online Library on [07/11/2026]. See the Terms and Conditions (https://onlinelibrary.wiley.com/terms-and-conditions) on Wiley Online Library for rules of use; OA articles are governed by the applicable Creative Commons License

38. G. Tian, W. Deng, Y. Gao, et al., "Rich Lamellar Crystal Baklava-Structured PZT/PVDF Piezoelectric Sensor Toward Individual Table Tennis Training," *Nano Energy* 59 (2019): 574–581, https://doi.org/10.1016/j.nanoen.2019.03.013.

39. Y. Liu, X. Chen, Z. Han, H. Zhou, and Q. Wang, "Defects in Poly(vinylidene fluoride)-based Ferroelectric Polymers From a Molecular Perspective," *Applied Physics Reviews* 9 (2022): 031306, https://doi.org/10.1063/5.0097446.

40. L. Huang, W. Deng, G. Tian, et al., "Low Electric Field-Driven and Fast-Moving Relaxor Ferroelectric Soft Robots," *InfoMat* 7 (2025): 70015, https://doi.org/10.1002/inf2.70015.

41. G. Tian, W. Deng, T. Yang, et al., "Insight Into Interfacial Polarization for Enhancing Piezoelectricity in Ferroelectric Nanocomposites," *Small* 19 (2023): 2207947.

42. H. Li, Y. Zhou, Y. Liu, L. Li, Y. Liu, and Q. Wang, "Dielectric Polymers for High-Temperature Capacitive Energy Storage," *Chemical Society Reviews* 50 (2021): 6369–6400, https://doi.org/10.1039/D0CS00765J.

43. T. R. Houpt, "Gastric Pressures in Pigs During Eating and Drinking," *Physiology & Behavior* 56 (1994): 311–317, https://doi.org/10.1016/0031-9384(94)90200-3.

44. H. Lei, Y. Chen, Z. Gao, Z. Wen, and X. Sun, "Advances in Self-Powered Triboelectric Pressure Sensors," *Journal of Materials Chemistry A* 9 (2021): 20100–20130, https://doi.org/10.1039/D1TA03505C.

45. S. H. Jeong, S. Zhang, K. Hjort, J. Hilborn, and Z. Wu, "PDMS-Based Elastomer Tuned Soft, Stretchable, and Sticky for Epidermal Electronics," *Advanced Materials* 28 (2016): 5830.

46. B. Zhang, J. Li, J. Zhou, et al., "A Three-Dimensional Liquid Diode for Soft, Integrated Permeable Electronics," *Nature* 628 (2024): 84–92, https://doi.org/10.1038/s41586-024-07161-1.

47. S. J. Park and T. Tamura, "Distribution of Evaporation Rate on Human Body Surface," *Annals of Physiological Anthropology* 11 (1992): 593–609, https://doi.org/10.2114/ahs1983.11.593.

48. J. A. Fan, W. H. Yeo, Y. Su, et al., "Fractal Design Concepts for Stretchable Electronics," *Nature Communications* 5 (2014): 3266.

49. J. Min, H. Ahn, H. Lukas, et al., "Continuous Biochemical Profiling of the Gastrointestinal Tract Using an Integrated Smart Capsule," *Nature Electronics* 8 (2025): 844–855, https://doi.org/10.1038/s41928-025-01407-0.

50. K. Liu, A. E. Biju, A. Alshareef, S. Liu, B. Kuo, and S. Srinivasan, "Gastrointestinal Neuromuscular Interfaces: Bioelectronic Device Design for Gastrointestinal Motility," *Device* 3 (2025): 100867, https://doi.org/10.1016/j.device.2025.100867.

51. S. Srinivasan, M. J. Antonini, A. Alshareef, et al., "Gastrointestinal Neuroprosthesis for Motility and Metabolic Neuromodulation," *Nature Communications* 16 (2025): 7374.

52. C. Dagdeviren, F. Javid, P. Joe, et al., "Flexible Piezoelectric Devices for Gastrointestinal Motility Sensing," *Nature Biomedical Engineering* 1 (2017): 807–817, https://doi.org/10.1038/s41551-017-0140-7.

53. H. Liu, S. S. You, Z. Gao, N. Hu, and Y. Zhao, "Next Generation of Gastrointestinal Electrophysiology Devices," *Nature Reviews Gastroenterology & Hepatology* 21 (2024): 457–458, https://doi.org/10.1038/s41575-024-00952-x.

## Supporting Information

Additional supporting information can be found online in the Supporting Information section.

**Supporting File**: adma74367-sup-0001-SuppMat.docx.



15214095, 2026, 53, Downloaded from https://advanced.onlinelibrary.wiley.com/doi/10.1002/adma.74367 by Jilin University, Wiley Online Library on [07/11/2026]. See the Terms and Conditions (https://onlinelibrary.wiley.com/terms-and-conditions) on Wiley Online Library for rules of use; OA articles are governed by the applicable Creative Commons License